Hindawi
Journal of Sensors
Volume 2021, Article ID 8856033, 13 pages
https://doi.org/10.1155/2021/8856033

Research Article

A Moving Path Tracking Method of the Thunderstorm Cloud Based on the Three-Dimensional Atmospheric Electric Field Apparatus

Xu Yang,[1,2] **Hongyan Xing**,[1,2] **Wei Xu**,[1,2] **and Xinyuan Ji**[1,2]

[1]*Collaborative Innovation Center for Meteorological Disaster Prediction and Evaluation, Nanjing University of Information Science and Technology, Nanjing 210044, China*
[2]*Jiangsu Key Laboratory of Meteorological Detection and Information Processing, Nanjing University of Information Science and Technology, Nanjing 210044, China*

Correspondence should be addressed to Hongyan Xing; xinghy@nuist.edu.cn

Received 27 September 2020; Revised 27 February 2021; Accepted 10 March 2021; Published 23 March 2021

Academic Editor: Stelios M. Potirakis

In order to obtain the position of thunderstorm cloud in real time and make it possible to track the thunderstorm cloud motion, a method is proposed for tracking the moving path of thunderstorm cloud, with the aid of the three-dimensional atmospheric electric field apparatus (AEFA). According to the method of images, we establish a spatial model for tracking the moving path. Based on the model, we define the dynamic parameters of thunderstorm cloud position. Subsequently, to realize the moving path tracking of thunderstorm cloud, its coordinates are associated with the time points. Besides, we use the relationship between electric field component measurement error, horizontal angle, elevation angle, and the tracking accuracy to analyze the tracking performance. Finally, a fusion system combining an electric field measurement unit, electric field calibration unit, and permittivity measurement unit is designed to meet the actual needs. The results show that the method can accurately track the thunderstorm cloud moving path and has a better effect. In addition, the method can also be combined with a radar map, thus better predicting the development of the thunderstorm cloud.

1. Introduction

Thunderstorm clouds are the main source of lightning [1, 2], while lightning is a major natural disaster. Lightning disasters have long been listed as one of the "ten worst natural disasters" by the relevant UN [3, 4]. Lightning is often accompanied by intense storms and gusts and sometimes by tornadoes and hail. According to estimates by the relevant departments, about 1,800 lightning strikes per minute around the world are in progress. They emit about 600 lightning bolts per second, of which 100 hit the Earth. Therefore, real-time and effective thunderstorm cloud monitoring methods are particularly important for improving lightning protection and disaster mitigation capabilities [5–7].

In the research of lightning forecasting and warning, AEFA has always played an important role. Based on AEFA, researchers have designed a one-dimensional AEFA and improved the lightning warning method [8–10]. However, these changes are still limited to a single measurement of the vertical electric field component, so the position of the thunderstorm cloud cannot be determined. Chen et al. [11] use the observation data of the ground electric field to perform quantum inversion of the thunderstorm cloud charge model and propose a charged disk thunderstorm cloud charge model. Frank-Kamenetsky et al. [12] study the global circuits formed by thunderstorms mainly occurring in the equatorial region. However, the data used in these experiments still comes from the near-surface vertical electric field component measured in Vostok, Russia, in 1998. Therefore, it is necessary to further study the horizontal electric field component, which is crucial for exploring the physical composition of the atmospheric electric field.

At present, AEFA has been widely used in the layout of sensitive units such as aerospace [13] and oil field

storage [14], and researchers are actively involved in its research work. Relevant studies find that the atmospheric electric field is composed of vertical and horizontal components [15–17]. In Ref. [15], the three-dimensional electric field sensor and the dielectric constant sensor are used to detect the spatial electric field, and a three-dimensional electric field system is proposed to conduct the electric field measurement. In Ref. [16], a three-dimensional AEFA is developed to simultaneously measure the electric field horizontal and vertical components, and a particle swarm optimization algorithm is introduced to invert the thunderstorm cloud orientation. In addition, electric field measurement and lightning warning data are used in Ref. [17] to prevent risks and damage to humans and sensitive systems. However, these studies cannot track the real-time moving path of the thunderstorm cloud, while realizing the electric field measurement. Therefore, the thunderstorm cloud forecasting warning cannot be achieved in the true sense.

The problem is that the real-time thunderstorm cloud localization cannot be well guaranteed. Therefore, this paper establishes a moving path tracking model for thunderstorm cloud. At the same time, the dynamic parameters of the thunderstorm cloud position are defined based on the model. According to the method of images, the calculation formulas of the three-dimensional electric field components are derived, and a moving path tracking method of the thunderstorm cloud is proposed. Then, the tracking performance is studied and the data measured by AEFA are used for the experiment. It is worth mentioning that to meet the practical needs, a fusion system is designed by combining an electric field measurement unit, electric field calibration unit, and permittivity measurement unit. Finally, we further combine the thunder source localization and radar echo map data to analyze the experimental results.

In this paper, the proposed moving path tracking method was used to locate the thunderstorm cloud in real time, and data collected were compared with theoretical data, radar chart data, and important literature. The results showed that by introducing the method, the three-dimensional AEFA could reproduce the path of the thunderstorm cloud movement. At the same time, the measured thunderstorm cloud position data could be used to provide data feedback for the radar echo map and could be used to predict the development of the thunderstorm cloud. In particular, the designed electric field measurement structure could modulate the electrostatic field, which effectively improved the measurement accuracy of the electric field.

The contributions of this paper are the following.

(1) In order to locate the thunderstorm cloud and track its motion, a moving path tracking model suitable for practical application is designed according to the relative position relationship between the thunderstorm cloud and three-dimensional AEFA

(2) An all-weather moving path tracking algorithm for the thunderstorm cloud is proposed. This method focuses on the establishment of the relationship between the position of the thunderstorm cloud point and time points. In other words, during the thunderstorm monitoring process, the movement information of thunderstorm cloud is acquired in real time

(3) We design a single-axis rotary vane-type AEFA. Compared with the traditional one-dimensional vibration shielding-type apparatus, the unique rotary vane structure can modulate the electrostatic field and complete the measurement of three-dimensional electric field components

2. Analysis of Thunderstorm Cloud Moving Path Tracking

2.1. Moving Path Tracking Model. Based on the three-dimensional coordinate system of AEFA, we simplify the thunderstorm cloud region into a point charge [5, 15, 16]. Besides, the moving path tracking model of the thunderstorm cloud is obtained as shown in Figure 1.

In Figure 1, the three-dimensional rectangular coordinate system is established with point N as the coordinate origin, and $N(0, 0, 0)$ is the position of the three-dimensional AEFA.$S_T(x_T, y_T, z_T)$ is the dynamic position of the thunderstorm cloud point S_T changing with time T. h represents the sum of the altitude of the apparatus and its position. α_T and β_T, respectively, are the dynamic horizontal and elevation angle of point S_T, and R_T is the real-time distance from point S_T to apparatus N. E_T is the real-time electric field intensity at the point S_T measured by apparatus N. Meanwhile, $E_{X,T}$, $E_{Y,T}$, and $E_{Z,T}$, respectively, are the electric field strengths of the thunderstorm cloud in the x-axis, y-axis, and z-axis directions measured by N, and the two are perpendicular to each other.

It can be seen from Figure 1 that when the thunderstorm cloud appears above the electric field apparatus, a large amount of charge will accumulate in the cloud. At this time, the electric field E_T generated by the thunderstorm cloud will be sensed by the 3D electric field sensor of the apparatus. After that, the coordinates of the thunderstorm cloud point can be obtained by calculation, which can provide a data source for tracking the moving path of the cloud. However, the classical thunderstorm detection model is mainly based on the field mill-type atmospheric electric field meter, as shown in Figure 2 [8–12].

In Figure 2, the point M represents the position of the field mill-type electric field meter. Different from Figure 1, after the vertical component of the atmospheric electric field is obtained by using this model, only the distance between the thunderstorm cloud and observation point and the degree of charge accumulation in the cloud can be roughly judged. In fact, the position of the thunderstorm cloud cannot be determined by using a one-dimensional electric field component, which leads to its

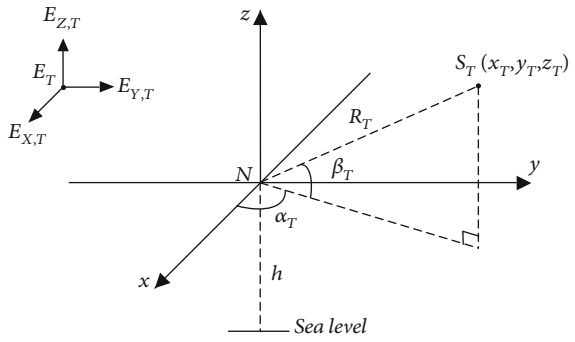

Figure 1: A spatial model for tracking the thunderstorm cloud moving path.

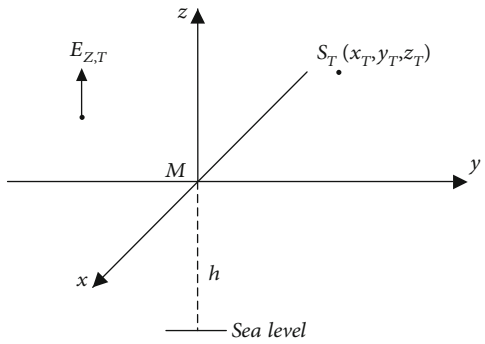

Figure 2: Model of electric field measurement based on a field mill-type atmospheric electric field meter.

low-precision thunderstorm warning ability in practical application. Figure 3 shows the difference between the two.

2.2. Moving Path Tracking Method. As time goes by, there will be irregular movements in the area where the thunderstorm cloud is located. Therefore, by detecting the location of the thunderstorm cloud to study the tracking method of the thunderstorm cloud moving path, this has an important practical significance for lightning forecasting and warning.

According to the theory that the induced charge is equal to mirror charge in the mirror image method [15, 16], the thunderstorm cloud area is regarded as a point charge q, and the real-time potential distribution φ_T of point S_T is obtained as follows at apparatus N:

$$\varphi_T = \frac{1}{4\pi\varepsilon_1}\left(\frac{q}{\sqrt{{x_T}^2+{y_T}^2+(z_T-h)^2}} - \frac{\varepsilon_2-\varepsilon_1}{\varepsilon_2+\varepsilon_1}\frac{q'}{\sqrt{{x_T}^2+{y_T}^2+(z_T+h)^2}}\right). \tag{1}$$

In Equation (1), q' is the image charge of the point charge q. In addition, ε_1 and ε_2, respectively, are the permittivity of the air and the ground where the apparatus N is located.

Since electric field intensity E_T measured by apparatus N is a three-dimensional vector, the orthogonal decomposition of E_T can be performed to get

$$E_T = E_{X,T} + E_{Y,T} + E_{Z,T}. \tag{2}$$

By taking derivatives of the potential distribution φ in the direction of x-, y-, and z-axes, $E_{X,T}$, $E_{Y,T}$, and $E_{Z,T}$ can be gotten:

$$\begin{cases} E_{X,T} = \dfrac{\partial\varphi_T}{\partial x_T} = \dfrac{-qx_T}{4\pi\varepsilon_1}\left\{\left[{x_T}^2+{y_T}^2+(z_T-h)^2\right]^{-3/2} - \dfrac{\varepsilon_2-\varepsilon_1}{\varepsilon_2+\varepsilon_1}\left[{x_T}^2+{y_T}^2+(z_T+h)^2\right]^{-3/2}\right\}, \\ E_{Y,T} = \dfrac{\partial\varphi_T}{\partial y_T} = \dfrac{-qy_T}{4\pi\varepsilon_1}\left\{\left[{x_T}^2+{y_T}^2+(z_T-h)^2\right]^{-3/2} - \dfrac{\varepsilon_2-\varepsilon_1}{\varepsilon_2+\varepsilon_1}\left[{x_T}^2+{y_T}^2+(z_T+h)^2\right]^{-3/2}\right\}, \\ E_{Z,T} = \dfrac{\partial\varphi_T}{\partial z_T} = \dfrac{-q}{4\pi\varepsilon_1}\left\{(z_T-h)\left[{x_T}^2+{y_T}^2+(z_T-h)^2\right]^{-3/2} - \dfrac{\varepsilon_2-\varepsilon_1}{\varepsilon_2+\varepsilon_1}(z_T+h)\left[{x_T}^2+{y_T}^2+(z_T+h)^2\right]^{-3/2}\right\}. \end{cases} \tag{3}$$

Usually, the thunderstorm cloud coordinate parameter z is usually two orders of magnitude higher than the height h [15–17]; then,

$$z_T \approx z_T - h \approx z_T + h. \tag{4}$$

According to Figure 1, the distance R_T from pointS_T to apparatus N is

$$R_T = \sqrt{{x_T}^2+{y_T}^2+{z_T}^2}. \tag{5}$$

Equations (4) and (5) are used to change Equation (3) to

$$\begin{cases} E_{X,T} = m(1-n){R_T}^{-3}x_T, \\ E_{Y,T} = m(1-n){R_T}^{-3}y_T, \\ E_{Z,T} = m(1-n){R_T}^{-3}z_T. \end{cases} \tag{6}$$

In Equation (6), $m = -q/4\pi\varepsilon_1$ and $n = (\varepsilon_2-\varepsilon_1)/(\varepsilon_2+\varepsilon_1)$.

Equation (6) is used to obtain the spherical coordinate $({R_T}', {\alpha_T}', {\beta_T}')$ of thunderstorm cloud point S_T changing with time T:

$$\begin{cases} {R_T}' = \sqrt[4]{\dfrac{m^2(1-n)^2}{{E_{X,T}}^2+{E_{Y,T}}^2+{E_{Z,T}}^2}}, \\ {\alpha_T}' = \arctan\dfrac{E_{Y,T}}{E_{X,T}}, \\ {\beta_T}' = \arctan\dfrac{\varepsilon_1 E_{Z,T}}{\varepsilon_2\sqrt{{E_{X,T}}^2+{E_{Y,T}}^2}}. \end{cases} \tag{7}$$

In Equation (7), ${R_T}'$ is the inversion value of distance R_T from thunderstorm cloud S_T to apparatus N and ${\alpha_T}'$ and ${\beta_T}'$ are the inversion values of thunderstorm cloud

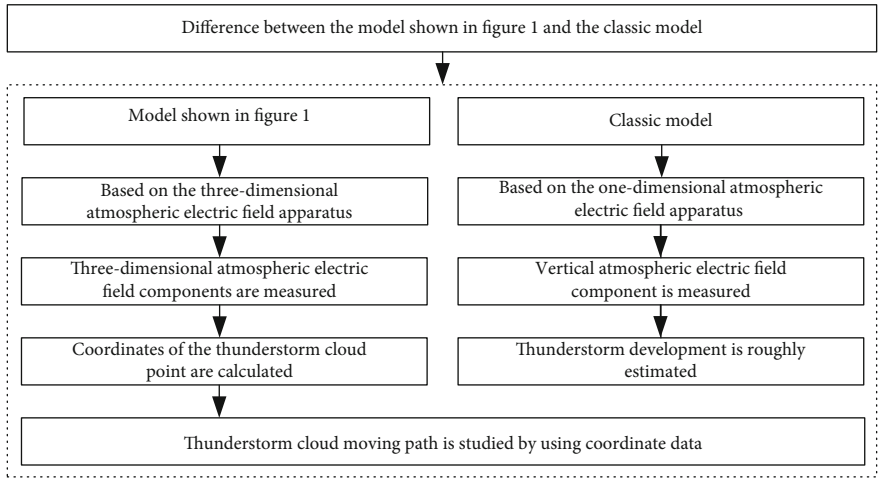

Figure 3: Comparison between the model in this paper and the classical model.

dynamic horizontal angle α_T and elevation angle β_T, respectively. When point charge q and permittivity $\varepsilon_1, \varepsilon_2$ are known, real-time thunderstorm cloud coordinates $(R_T{}', \alpha_T{}', \beta_T{}')$ are only related to three-dimensional electric field vectors $E_{X,T}$, $E_{Y,T}$, and $E_{Z,T}$. Once $E_{X,T}$, $E_{Y,T}$, and $E_{Z,T}$ are determined, the moving path of the thunderstorm cloud can be further explored.

The set P of thunderstorm cloud dynamic coordinates that change with time T is defined as

$$P = \left\{ \left(R_T{}', \alpha_T{}', \beta_T{}'\right) \middle| \left(R_{T_1}{}', \alpha_{T_1}{}', \beta_{T_1}{}'\right), \left(R_{T_2}{}', \alpha_{T_2}{}', \beta_{T_2}{}'\right), \cdots \left(R_{T_n}{}', \alpha_{T_n}{}', \beta_{T_n}{}'\right) \right\}. \tag{8}$$

In Equation (8), $T_1, T_2, \cdots T_n$ refer to the first, second, $\cdots$, n-th time points, respectively, and the corresponding thunderstorm cloud coordinates are $(R_{T_1}{}', \alpha_{T_1}{}', \beta_{T_1}{}')$, $(R_{T_2}{}', \alpha_{T_2}{}', \beta_{T_2}{}')$, $\cdots (R_{T_n}{}', \alpha_{T_n}{}', \beta_{T_n}{}')$, respectively.

After Equations (7) and (8) are combined, if the thunderstorm cloud position is associated with the time point, the thunderstorm cloud moving path tracking can be realized.

3. Performance Analysis of the Thunderstorm Cloud Moving Path Tracking Method

According to the electric field distribution of air charge [15, 18] and the charge structure of thunderstorm clouds [16, 19], air permittivity ε_1 is set as 1, the permittivity ε_2 of the ground where the apparatus N is located is set as 5, and the charge amount q is set as 5. In addition, the standard deviation of the atmospheric electric field measurement components is set as σ_{E_i} to study the overall performance of the tracking method.

The thunderstorm cloud coordinate formula is the basis of its moving path tracking method. According to the indirect measurement error theory [20–22], measurement error σ_R, σ_α, σ_β of distance $R_T{}'$, horizontal angle $\alpha_T{}'$, and elevation angle $\beta_T{}'$ caused by electric field component measurement error σ_{E_i} can be obtained by Equation (7):

$$\begin{cases} \sigma_R = \sqrt{\left(\dfrac{\partial R_T{}'}{\partial E_{X,T}}\right)^2 \sigma_{E_i}{}^2 + \left(\dfrac{\partial R_T{}'}{\partial E_{Y,T}}\right)^2 \sigma_{E_i}{}^2 + \left(\dfrac{\partial R_T{}'}{\partial E_{Z,T}}\right)^2 \sigma_{E_i}{}^2}, \\ \sigma_\alpha = \sqrt{\left(\dfrac{\partial \alpha_T{}'}{\partial E_{X,T}}\right)^2 \sigma_{E_i}{}^2 + \left(\dfrac{\partial \alpha_T{}'}{\partial E_{Y,T}}\right)^2 \sigma_{E_i}{}^2 + \left(\dfrac{\partial \alpha_T{}'}{\partial E_{Z,T}}\right)^2 \sigma_{E_i}{}^2}, \\ \sigma_\beta = \sqrt{\left(\dfrac{\partial \beta_T{}'}{\partial E_{X,T}}\right)^2 \sigma_{E_i}{}^2 + \left(\dfrac{\partial \beta_T{}'}{\partial E_{Y,T}}\right)^2 \sigma_{E_i}{}^2 + \left(\dfrac{\partial \beta_T{}'}{\partial E_{Z,T}}\right)^2 \sigma_{E_i}{}^2}. \end{cases} \tag{9}$$

Equation (9) is further simplified, and we can get

$$\begin{cases} \sigma_R = \dfrac{6}{5}\pi^{3/2} R_T{}'^3 \sigma_{E_i}, \\ \sigma_\alpha = \dfrac{12}{5}\pi R_T{}'^2 \sqrt{1 + 25\tan^2\beta_T{}'}\,\sigma_{E_i}, \\ \sigma_\beta = \dfrac{12}{25}\pi R_T{}'^2 \cos\beta_T{}' \cdot \sqrt{\left(1 + 24\sin^2\beta_T{}'\right)\left(1 + 25\tan^2\beta_T{}'\right)}\,\sigma_{E_i}. \end{cases} \tag{10}$$

In Equation (10), ranging error σ_R of the tracking method is only related to distance $R_T{}'$ and electric field measurement error σ_{E_i}, independent of thunderstorm cloud horizontal angle $\alpha_T{}'$ and elevation angle $\beta_T{}'$. In addition, direction-finding errors σ_α and σ_β are related to distance $R_T{}'$, elevation angle $\beta_T{}'$, and electric field measurement error σ_{E_i}, but they are independent of angle $\alpha_T{}'$.

Therefore, in practical application, the performance of the tracking method is not affected by the change of horizontal deviation angle. Within the maximum measuring range of three-dimensional AEFA, the smaller the distance $R_T{}'$ and the electric field measurement error σ_{E_i} are, the higher the ranging and direction finding accuracy of this method will be.

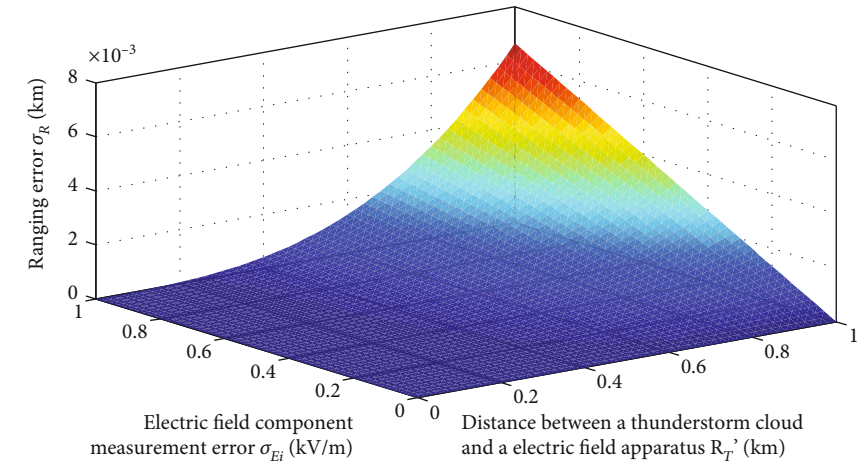

Figure 4: Analysis diagram of ranging error.

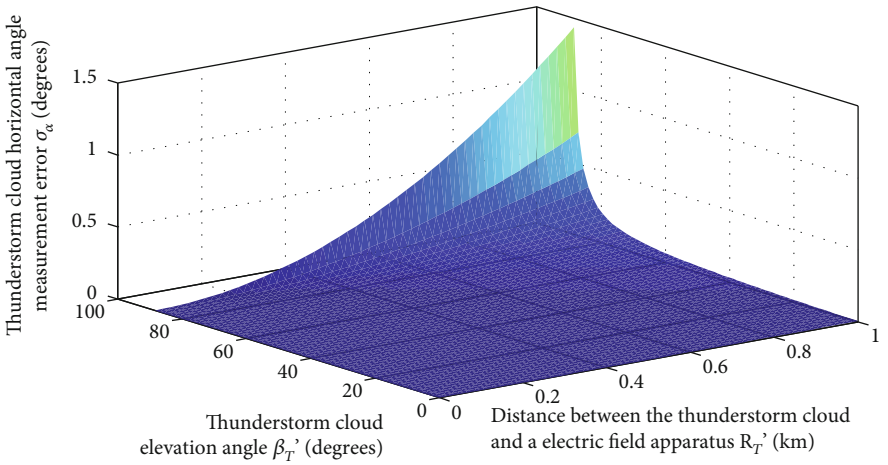

Figure 5: Analysis diagram of horizontal angle measurement error.

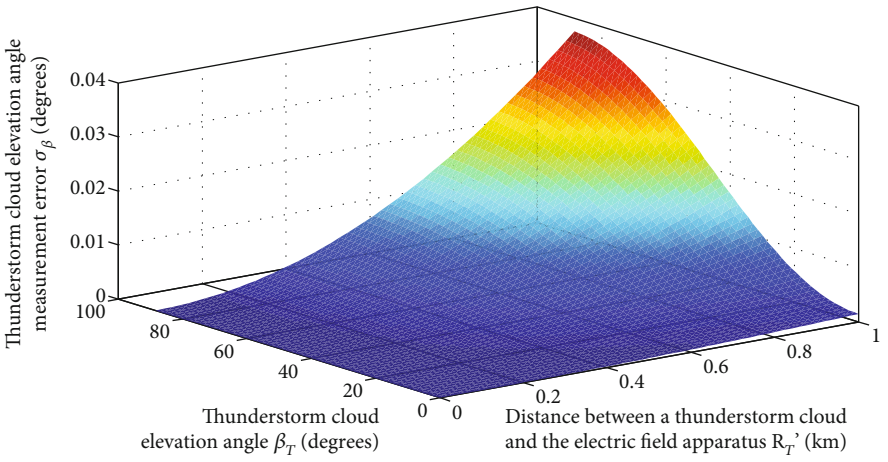

Figure 6: Analysis diagram of elevation angle measurement error.

3.1. Analysis of Ranging Performance. Equation (10) is used to study the relationship between distance $R_T{}'$, electric field measurement error σ_{E_i}, and ranging error σ_R of the tracking method, and the simulation results are shown in Figure 4.

In Figure 4, ranging error σ_R of the tracking method increases with the increase in distance $R_T{}'$ and electric field measurement error σ_{E_i}. When distance $R_T{}'$ is between 0 and 0.55 km, ranging error σ_R is less affected by electric field

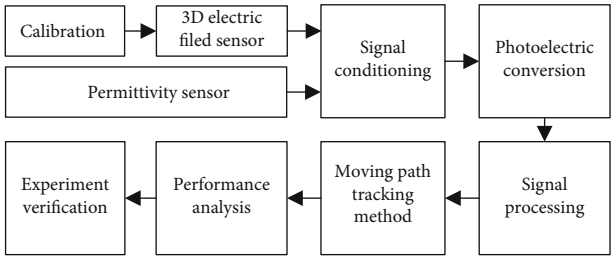

Figure 7: Schematic diagram of the system framework.

measurement error σ_{E_i} and $\sigma_{R\max}$ only reaches 1 m. However, when distance $R_T{}'$ is greater than 0.55 km, ranging error σ_R increases abruptly with the increase in error σ_{E_i} and $\sigma_{R\max}$ reaches 6.4 m. Similarly, when electric field measurement error σ_{E_i} is smaller than 0.15 kV/m, ranging error σ_R is less affected by distance $R_T{}'$ and $\sigma_{R\max}$ only reaches 1 m. However, when electric field measurement error σ_{E_i} ranges from 0.15 to 1 kV/m, the error σ_R rises to 6.4 m as distance $R_T{}'$ increases. In conclusion, although ranging error σ_R of this method is inevitable, it is still within the acceptable range and shows good tracking ranging performance.

From Figure 4, it is found that the maximum ranging error is only 6.4 m for tracking within a limited range. Assuming that a thunderstorm cloud is at a very remote location, this obviously exceeds the thunderstorm cloud detection range of the apparatus, which will inevitably produce a large number of levels of error. This is intuitively reflected in Figure 4. Therefore, if each apparatus is regarded as a test point, the ranging error will be very small when measured within the effective range.

3.2. Analysis of Direction Finding Performance. Equation (10) is used to study the relationship between distance $R_T{}'$, thunderstorm cloud elevation angle $\beta_T{}'$, and its horizontal angle measurement error σ_α, and the simulation results are shown in Figure 5.

In Figure 5, horizontal angle measurement error σ_α of the tracking method increases with the increase in distance $R_T{}'$ and elevation angle $\beta_T{}'$. When distance r' is 0 to 0.42 km, measurement error σ_α is less affected by elevation angle $\beta_T{}'$ and error σ_α is less than 0.2 degree; however, when distance r' is greater than 0.42 km, measurement error σ_α increases exponentially with the increase in elevation angle $\beta_T{}'$ and $\sigma_{\alpha\max}$ reaches 1.07 degrees. When distance $R_T{}'$ and angle $\beta_T{}'$ are both large, error σ_α increases sharply with the increase in the two. In most cases, though, error σ_α is hardly affected by either.

Once again, Equation (10) is used to study the relationship between distance $R_T{}'$, thunderstorm cloud elevation angle $\beta_T{}'$, and its elevation angle measurement error σ_β, and the simulation results are shown in Figure 6.

In Figure 6, elevation angle measurement error σ_β of the tracking method increases with the increase in distance $R_T{}'$ and elevation angle $\beta_T{}'$; when distance $R_T{}'$ is 0 to 0.35 km, elevation angle measurement error σ_β is less affected by elevation angle $\beta_T{}'$ and $\sigma_{\beta\max}$ only reaches 0.005 degree; when distance $R_T{}'$ is greater than 0.35 km, measurement error σ_β slowly climbs to 0.0375 degree as elevation angle $\beta_T{}'$ increases. Similarly, when elevation angle $\beta_T{}'$ is less than 30 degrees, error σ_β is hardly affected by distance $R_T{}'$ and $\sigma_{\beta\max}$ only reaches 0.01 degree. However, when distance $R_T{}'$ and elevation angle $\beta_T{}'$ are both large, measurement error σ_β only rises to 0.0375 degree too.

When the target thunderstorm cloud is far away from the apparatus, its negative impact is not limited to the ranging accuracy of the method but also affects its direction finding accuracy. It can be easily seen in conjunction with Figures 5 and 6 that once the limit detection range of the apparatus is exceeded, the curve caused by this negative influence becomes more and more dramatic, and the error increases significantly. However, although the direction finding error cannot be avoided, the magnitude of the error is small and still controllable.

The overall direction finding performance of the thunderstorm cloud moving path tracking method is good. In actual experiments, the algorithms such as data fusion and precision compensation can be introduced to reduce the negative impact of this kind of nonlinear behavior on the performance of thunderstorm cloud location.

4. Structure Design

In order to track the moving path of thunderstorm cloud, a fusion system is obtained by combining a three-dimensional atmospheric electric field measurement unit, electric field calibration unit, and permittivity measurement unit. The schematic diagram is shown in Figure 7.

In Figure 7, the two sensors first convert physical signals into electrical signals. Then, through signal conditioning and photoelectric conversion, the electrical signals are converted into digital signals. Furthermore, the signals are sent to the main control system for processing. After introducing the moving path tracking method, the performance of the method is analyzed. Finally, the effectiveness of the method is verified by the actual experiments in different weather conditions.

4.1. Electric Field Measurement Unit. The structure of the three-dimensional electric field sensor, which is designed based on the electrostatic induction principle, is illustrated in Figure 8 [15–17].

In Figure 8, the single-axis rotary vane structure mainly consists of a rotating blade, an induction electrode Z perpendicular to the z-axis, sensing electrodes X and Y surrounding and parallel to the z-axis, a photoelectric switch, a synchronous blade, and a motor. The z-axis direction is alternately arranged by two sets of sensing sheets, and the sensing electrodes X and Y are composed of two opposite rectangular metal plates distributed on the side of the cylinder body. The sensing electrode Z is a metal disk that is equally divided into eight sector

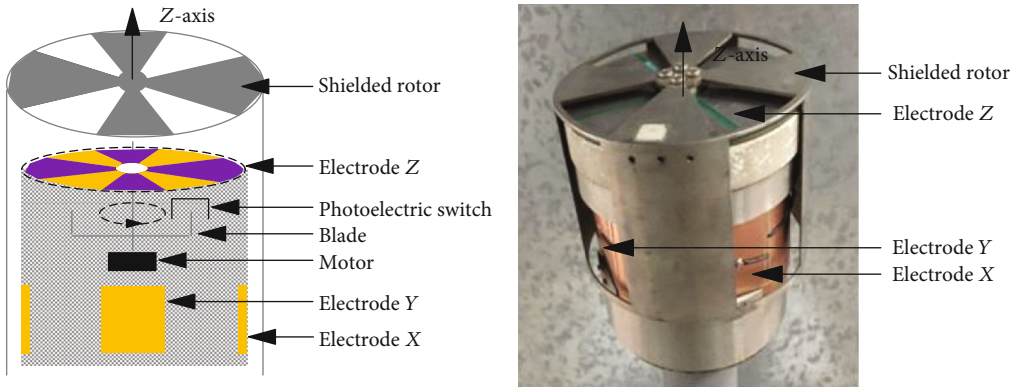

(a) The schematic diagram (b) The photograph

FIGURE 8: A single-axis rotary vane structure for electric field measurement.

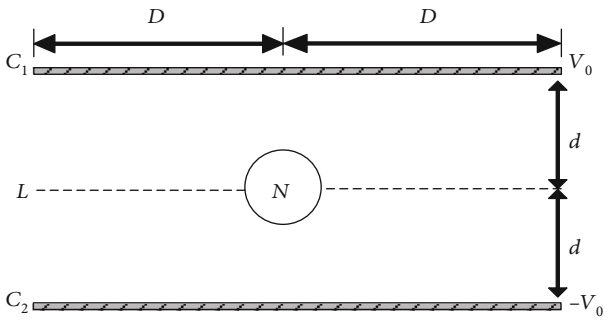

FIGURE 9: Calibration diagram of the electric field.

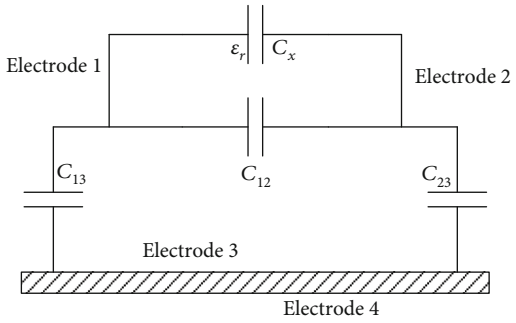

FIGURE 10: Equivalent circuit of a permittivity measurement device.

TABLE 1: Performance parameters of the system.

Parameter type	Specific value
Power	DC voltage 12 V
Electricity consumption	<15 W
Temperature and humidity	-25~85°C, 0~100% RH
Measurement radius	<15 km
Electric field measurement range	-50 kV/m~50 kV/m
Direction finding error	<10%
False alarm rate	<10%

regions. When the motor drives the shield to rotate at a constant speed, the electrodes X, Y, and Z and the atmospheric electric field are periodically shielded and contacted, and an induced current is generated at each electrode. In the meanwhile, the blade is continuously driven by the motor. The photoelectric switch is fixed on the back side of electrode Z. When it rotates synchronously with the shield electrodes, the metal part of the blade cuts the photoelectric switch optical path and the hollow portion does not block the optical path, thereby generating a square wave signal synchronized with the modulated electric field. It is convenient for phase-sensitive detection of the induced voltage.

Since the traditional one-dimensional AEFA has only one electrode Z and a corresponding rotating shield at the bottom of the cylinder, this apparatus can only measure the vertical component of the atmospheric electric field. Moreover, this kind of electric field apparatus only works well on sunny days, because the horizontal electric field components are very weak and can be neglected. Horizontal components are closely related to the thunderstorm cloud position, so they cannot be ignored. Compared with the one-dimensional electric field apparatus, the three-dimensional electric field measurement structure shown in Figure 8 can measure not only the vertical electric field component but also the horizontal electric field components, which cannot be realized by the traditional electric field apparatus.

4.2. Electric Field Calibration Unit. To ensure the accuracy of measured electric field data, we implement the calibration of the electric field apparatus before the experiments. Building a known standard uniform electric field is the key to effective calibration. For this, a uniform electric field is generated by using two parallel plate capacitors as shown in Figure 9.

In Figure 9, the upper and lower parallel electrode plates C_1 and C_2 are both square thin metal plates, and the distance between the two plates is $2d$. The electric field apparatus N is located on the center line L between the two parallel plates, and the distance from its center

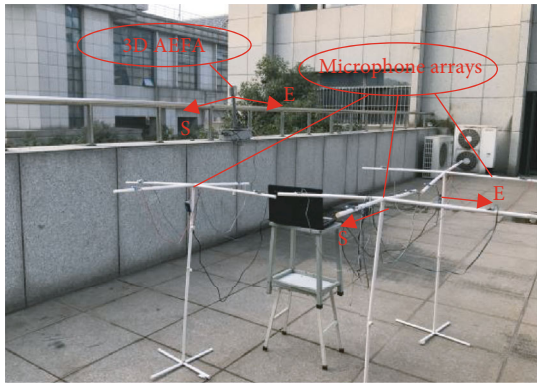

Figure 11: Arrangement of AEFA and microphone arrays.

Table 2: The experiment on April 9, 2019.

Time point T	$(E_{X,T}, E_{Y,T}, E_{Z,T})$ (kV/m)	Coordinates (km, degrees, degrees)
10:06	(-0.015, 0.022, 0.425)	(0.558, -55.71, 72.61)
10:33	(0.019, 0.030, 0.398)	(0.576, 57.65, 65.96)
10:50	(0.023, 0.038, 0.377)	(0.591, 58.82, 59.50)
11:07	(0.031, 0.046, 0.343)	(0.618, 146.02, 51.04)

position to the plate edge is D. After adding DC voltages of V_0 and $-V_0$ to the two plates, the uniform electric field value generated between the two plates is

$$E = \frac{V_0 - (-V_0)}{2d} = \frac{V_0}{d}. \tag{11}$$

After voltages V_0 and $-V_0$ are input into the parallel electrode plates, uniform electric fields of different intensity are generated by adjusting the voltages. On the one hand, after the real-time voltage value is measured by the data collector, the theoretical value of the electric field intensity can be calculated between the plates, according to distance $2d$ between the plates. On the other hand, an electric field sensor is used to convert the electric field value between the plates into a direct current voltage signal. Finally, by comparing the theoretical and measured values, the calibration of the electric field can be achieved.

4.3. Permittivity Measurement Unit. Considering the inconvenience of sampling and real-time measurement, a device which can ensure the measurement accuracy of the permittivity contained in Equation (1) is put forward by using a coplanar electrode sensor. The equivalent circuit of the device is shown in Figure 10.

In Figure 10, ε_r represents the permittivity. The device mainly includes the coplanar capacity sensor with 4 electrodes. Among them, electrodes 1 and 2 are the measurement electrodes and electrodes 3 and 4 are the shielding electrodes. The latter two electrodes are connected to the ground to shield the interference of the environmental electric field. The capacitance C_x is the measured capacitance between electrode 1 and electrode 2. On the one hand, the difference ΔC of the capacitance C_x and C_{air} is the linear function of measuring material permittivity. On the other hand, the capacitance values C_{12}, C_{13}, and C_{23} are fixed and can be eliminated during measurement. Therefore, the permittivity ε_r can be calculated as follows:

$$\varepsilon_r = \frac{\Delta C}{C_{\text{air}}} + 1. \tag{12}$$

The principle of the device is that the capacitance will change with the different filling media between the electrodes. Specifically, placing the object to be measured in the measurement area of the sensor will change the capacitance of the sensor. Then, the relative permittivity of the object is calculated from the measured capacitance variation. This method is suitable for hard solids such as rock and concrete, which are difficult to sample, and also suitable for monitoring soil, sand, and other substances whose relative permittivity changes due to rain.

4.4. Performance Parameter. The system can track the moving path of thunderstorm cloud with a radius of 15 km, and the error of ranging and direction finding is less than 10%. The specific performance parameters are shown in Table 1.

5. Experimental Results and Analyses

The three-dimensional AEFA^N at the test point of Nanjing University of Information Science & Technology (NUIST) is installed in the School of Electronic and Information Engineering. The electric field apparatus is placed in the same place as the microphone array used for locating the thunder source [22–24], as shown in Figure 11. Here, the apparatus is about 28 m away from the average sea level. In the three-dimensional coordinate system of N, it is defined that the x-axis positive axis is south and the y-axis positive axis is east. To obtain the set P (units: km, degrees, and degrees) composed of thunderstorm cloud point charge coordinates $(R_T', \alpha_T', \beta_T')$, we use the three-dimensional electric field component value $(E_{X,T}, E_{Y,T}, E_{Z,T})$ (unit: kV/m) recorded by the host computer interface. In addition, P is compared with the thunder source localization and radar echo map data.

In Figure 11, the maximum measurement distance of AEFA is between 10 and 20 km. In addition, its data sampling rate is 250 times per second, and it can ensure the output of three-dimensional electric field component mean value every minute.

5.1. An Experiment in Rainy Weather. From 10:06 to 11:07 on April 9, 2019, the electric field component data (unit: kV/m) measured by AEFA are shown in Table 2.

In Table 2, $E_{Z,T}$ is larger than $E_{X,T}$ and $E_{Y,T}$. By observing the data shown in Table 2, it can be initially determined that between 10:06 and 11:07, there may be lightning activity in the area above the NUIST station. However, due to the lack of correlation between the electric field component and other physical quantities, the

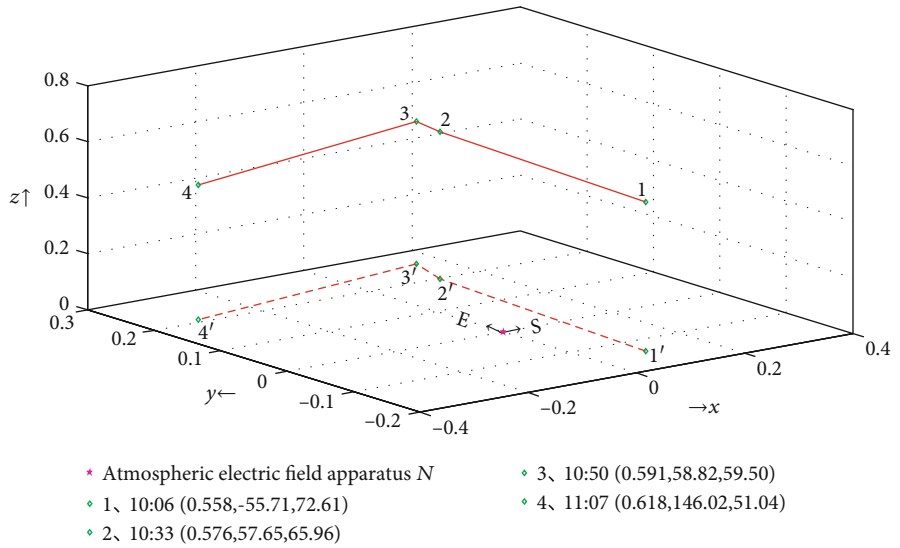

Figure 12: The real-time tracking chart of the thunderstorm cloud moving path on April 9, 2019.

Table 3: The thunder source localization experiment on April 9, 2019.

Time	Spherical coordinates (km, degrees, degrees)
10:42	(0.652, 52.14, 79.38)

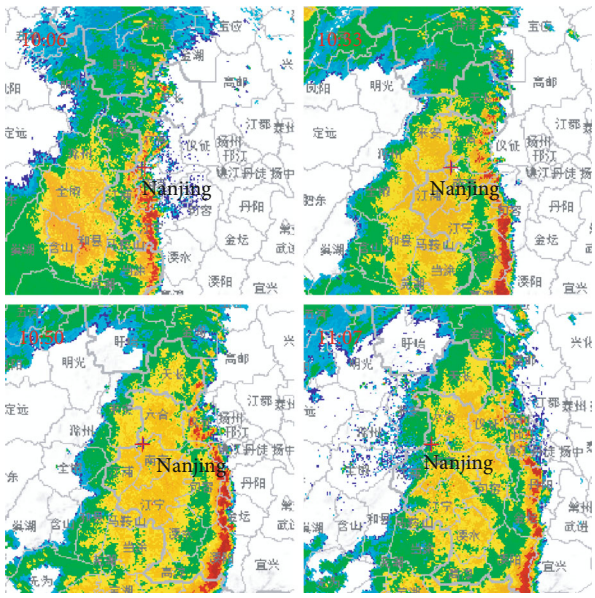

Figure 13: The radar echo map of the Nanjing radar station on April 9, 2019.

thunderstorm cloud moving path cannot be detected. Finally, the real-time forecasting and warning of thunderstorm clouds cannot be realized.

Therefore, we use the data in Table 2 and introduce the tracking method of the thunderstorm cloud moving path. The real-time tracking map is further obtained by associating time point T_n with the position $(R_T{}', \alpha_T{}', \beta_T{}')$ of the thunderstorm cloud, as shown in Figure 12.

In Figure 12, from point 1 to point 4 is the thunderstorm cloud moving path from 10:06 to 11:07 and from point $1'$ to point $2'$ to point $3'$ to point $4'$ is its path projected onto the $X0Y$ plane. As can be seen from Figure 12, at 10:06, (0.558, -55.71, 72.61) is the thunderstorm cloud coordinates measured by the apparatus. Thunderstorm cloud point S_T is about 55.71 degrees southwest, 0.558 kilometers. At this time, the thunderstorm cloud has a large elevation angle of 72.61 degrees. From 10:06 to 10:33, the thunderstorm cloud moves roughly 57.65 degrees from the southwest to the southeast and is 0.576 km above AEFA. From 10:33 to 10:50, the thunderstorm cloud point barely moved, staying above the 0.591 km southeast of the NUIST test point. Shortly after 10:50, the thunderstorm cloud moves to the northeast at 56.02 degrees at 11:07, and the thunderstorm cloud point is about 0.618 kilometers from AEFA. At this point, the elevation angle drops to 51.04 degrees, indicating that the thunderstorm cloud is moving away from the test point. In summary, the experimental time is in the spring season. Combined with Figure 12, in the airspace field of the test point, this method is used to reproduce the process of the thunderstorm cloud from the beginning to the end, which better verifies the effectiveness of the method.

In addition, we also use the microphone arrays shown in Figure 11 to locate the thunder source during the same time period. The resulting data are then compared to the tracking method. In addition, the array element spacing is set to 0.8 m. The sound source localization algorithm is introduced from Ref. [22], and the results shown in Table 3 are obtained by analyzing the thunder source signal.

In Table 3, (0.652, 52.14, 79.38) is the sound source coordinates measured by the microphone arrays at 10:42.

Table 4: The experiment on April 22, 2019.

Time point T	$(E_{X,T}, E_{Y,T}, E_{Z,T})$ (kV/m)	Coordinates (km, degrees, degrees)
20:43	(-0.054, 0.073, 0.126)	(0.924, 126.49, 15.51)
20:54	(-0.041, 0.066, 0.098)	(1.030, 121.85, 14.16)
21:05	(0.045, 0.057, 0.087)	(1.082, 51.71, 13.47)
21:16	(0.038, 0.052, 0.077)	(1.150, 53.84, 13.45)

The sound source is 52.14 degrees east-south, 0.652 km from the array center. In particular, its elevation angle is 79.38 degrees, almost perpendicular to the z-axis. At this time, it is considered that the thunder source has occurred in the upper area of the NUIST test point. In addition, between 10:33 and 10:50, 58 and 63 degrees, respectively, are the thunderstorm cloud horizontal and elevation angle measured by the tracking method, and the two shown in Table 3, respectively, are 52.14 and 79.38 degrees. Because the algorithm in Ref. [22] performs well in ranging, its elevation angle measurement performance is slightly inferior to that of its horizontal angle, resulting in a relatively large measurement error of the former. This can also be found by data comparative analysis of the two methods. Overall, this tracking method has better accuracy than Ref. [22].

To further prove the effectiveness of the tracking method, it can be compared with the official data measured by the Nanjing radar station. The radar echo map identical to the time point of Table 2 is selected, as shown in Figure 13. In addition, the red cross center marked in the radar chart is the NUIST test point.

It can be seen from Figure 13 that from 10:06 to 11:07, the radar echo intensity in the area above the NUIST test point is not less than 40 dBZ and the highest even reaches 55 dBZ. This indicates that a large amount of charge accumulates in the cloud above the test point, and there is indeed a thunderstorm cloud in this area. Through analysis, it is found that from 10:06, the thunderstorm cloud starts to approach the test point from the west and the radar echo intensity is always large. Besides, the thunderstorm area completely covers the test point. Subsequently, the thunderstorm cloud moves from the southwest to the east and continues to move until 11:07. After the thunderstorm cloud area moves away from the test point to the northeast, the radar echo intensity decreases. As shown in Figures 12 and 13, in this rainy weather experiment, the thunderstorm area rapidly moves from the southwest to the northeast of the test point. During this period, the thunderstorm cloud movement is consistent with the tracking method results.

5.2. An Experiment in Sunny Weather. From 20:43 to 21:16 on April 22, 2019, the electric field component data (unit: kV/m) measured by AEFA are shown in Table 4.

In Table 4, during the period from 20:43 to 21:16, since the electric field component $E_{Z,T}$ and elevation angle β_T are relatively small, it can be preliminarily judged that there is no lightning activity in the area above the NUIST test point. Similarly, the results of the tracking method are shown in Figure 14.

In Figure 14, from point 1 to point 2 to point 3 to point 4 is the thunderstorm cloud moving path from 20:43 to 21:16 and from point $1'$ to point $2'$ to point $3'$ to point $4'$ is its path projected onto the $X0Y$ plane. It can be seen from Figure 14 that at 20:43, thunderstorm cloud point S_T is about 53.51 degrees east-north. At this point, although the distance from the thunderstorm cloud to AEFA is about 0.924 km, the elevation angle is only 15.51 degrees. This indicates that there is no thunderstorm cloud in the area above the NUIST test point. From 20:43 to 20:54, the thunderstorm cloud is still northeast and 1.03 km away from AEFA, gradually moving away from AEFA. From 20:54 to 21:05, the thunderstorm cloud moves rapidly from the northeast 53.51 degrees to the southeast 51.71 degrees and stays at 1.082 km from the NUIST site. After 21:05, the thunderstorm cloud continues to move southeast. At 21:16, the thunderstorm cloud reaches 53.84 degrees south by east. At this point, it is 1.15 km away from AEFA. Throughout the process, the thunderstorm cloud is far from AEFA, and its elevation angle is small. This shows that there is no thunderstorm cloud over the test point. In addition, the method tracks the frequent activity of the thunderstorm cloud, in the eastern region about 1 km away from AEFA, which can predict that the thunderstorm cloud will continue to move in the southeast direction.

The microphone arrays in Figure 11 are used again, and the thunder source localization is carried out in the same time period. The results are shown in Table 5.

In Table 5, (0.143, -24.81, 35.06) are the sound source coordinates measured at 21:08. The sound source is in the direction of 24.81 degrees southwest, and its elevation angle is 35.06 degrees. In particular, the distance from the sound source to the array center is only 143 meters. This means that the sound source should be a certain interference source, not the target thunder source. Therefore, there is no thunderstorm cloud in the area above the NUIST test point. To provide information feedback for the moving path tracking method, we use the sound source localization algorithm, which helps to improve the accuracy of the thunderstorm cloud forecasting warning.

To further verify the effectiveness of the tracking method, we select the radar echo map data shown in Figure 15 with the same time point as in Table 4. Similarly, the red cross center marked in Figure 15 is the test point.

In Figure 15, from 20:43 to 21:16, the radar echo intensity is as low as 5 dBZ and the highest is only 20 dBZ, in the area above the NUIST test point. This indicates that a small charge amount has accumulated in the cloud above the test point, and there is no thunderstorm cloud in the area. Nevertheless, Figure 15 can still be used to verify the prediction of the results shown in Figure 14. Through observation, we find that in the eastern part far from AEFA, there is a large range of thunderstorm cloud area, and the radar echo intensity is as high as 45 dBZ. As time goes by, the thunderstorm cloud area gradually moves away from the test point and moves towards Yixing City, the southern city of Jiangsu. In conjunction with

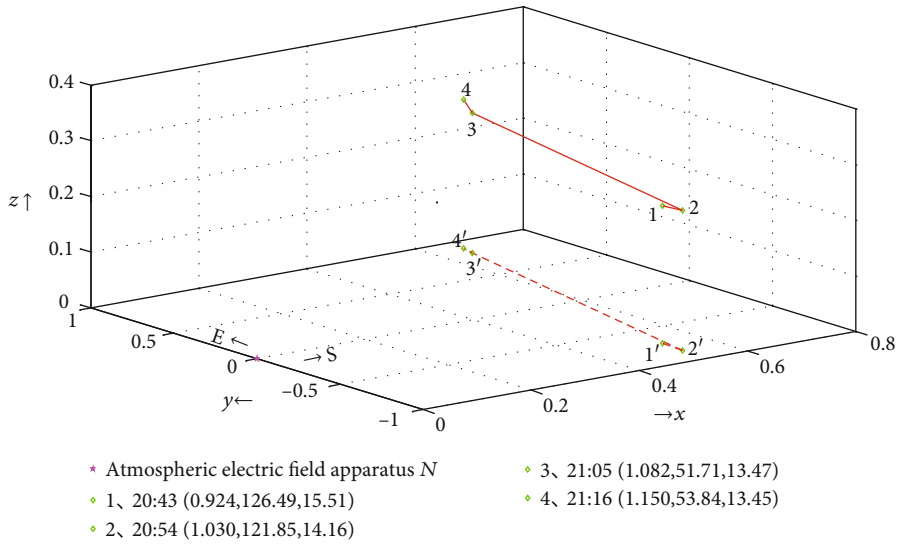

Figure 14: The real-time tracking chart of the thunderstorm cloud moving path on April 22, 2019.

Table 5: The thunder source localization experiment on April 22, 2019.

Time	Spherical coordinates (km, degrees, degrees)
21:08	(0.143, -24.81, 35.06)

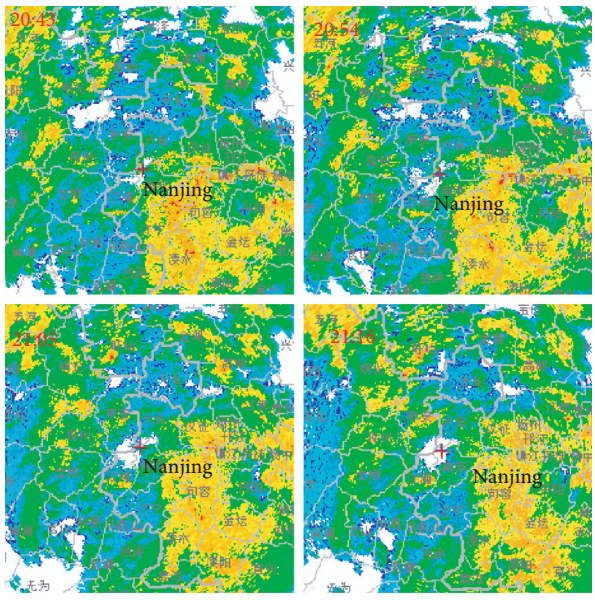

Figure 15: The radar echo map of the Nanjing radar station on April 22, 2019.

Figure 15, the motion of the thunderstorm cloud during this period is consistent with the results measured by the tracking method. As shown in Figures 14 and 15, in this sunny weather experiment, even if the thunderstorm cloud area does not cover the area above the test point, it is still within the tracking range. This is a good clarification of the tracking method effectiveness.

5.3. Contrast Experiments. To further verify the effectiveness of the tracking method, it is compared with References [5, 16]. Because the tracking method and references [5, 16] are based on the method of images, it is feasible to use the data measured by AEFA for comparative analysis.

In order to explore the influence of an algorithm on the thunderstorm cloud localization performance under the same condition, we further select the data measured under rainy weather as shown in Figure 12 and compared it with the data shown in Table 1 in Ref. [5] and Figure 4 in Ref. [16]. The contrast results are shown in Table 6.

In Table 6, in terms of electric field component measurement, all three perform well. Compared to Ref. [5] and the tracking method, although Ref. [16] can measure the electric field components, the thunderstorm cloud position cannot be further measured because the relationship between the electric field components and the position parameters is not found. In terms of performance analysis, the particle swarm optimization algorithm in Ref. [16] is used to compensate for the accuracy of thunderstorm cloud localization, which plays an active role in exploring the internal structural of thunderstorm cloud. However, the application effect of this algorithm has not been verified, and References [5, 16] do this better. In particular, thunderstorm cloud coordinates and time points are correlated in real time by the tracking method, making thunderstorm cloud motion tracking possible, which is not achieved in both References [5, 16].

Although the existing methods can realize the thunderstorm cloud localization, the lack of continuous thunderstorm cloud position monitoring makes the measured results lack correlation, and some results may be accidental. Therefore, real-time thunderstorm cloud moving path tracking cannot be achieved, and it is difficult to accurately monitor the time period after the thunderstorm cloud.

Table 6: The comparison with references [5, 16].

Data source	Electric field components	Thunderstorm cloud position	Performance analysis	Moving path tracking
Tracking method	Table 2	Figure 12	Equation (10)	Figure 12
Ref. [5]	Table 1	Table 1	Equation (11)	—
Ref. [16]	Figure 4	—	—	—

6. Conclusions

The three-dimensional electric field component produced by the thunderstorm cloud is real. By exploring the relationship between the electric field component and the physical quantity of the thunderstorm cloud position, we can make it possible to track the moving path of the thunderstorm cloud. Therefore, we correlate the thunderstorm cloud coordinates with the time point. At the same time, based on three-dimensional atmospheric electric field apparatus, we establish a moving path tracking model of the thunderstorm cloud and propose a tracking method. Finally, we carry out the experiments at the NUIST test point. The validity of the tracking method is verified by combining the thunder source localization and radar echo map.

These researches can not only realize the thunderstorm cloud localization but also complete its real-time moving path tracking. In a real sense, the thunderstorm cloud forecast and warning can be well achieved. Of course, thunderstorm monitoring involves many problems. For further accuracy improvement of the thunderstorm cloud motion tracking, what we need to do next is how to set up its network observation system.

Data Availability

The data are measured by the 3D atmospheric electric field apparatus developed by our team, and the authenticity of the data can be guaranteed.

Conflicts of Interest

The authors declare that there are no conflicts of interest regarding the publication of this paper.

Acknowledgments

This research is supported by the National Key Research and Development Program of China (Grant Nos. 2019YFE012990 and 2018YFC1506102), the National Natural Science Foundation of China (Grant Nos. 61671248 and 41605121), the Key Research and Development Plan of Jiangsu Province, China (Grant No. BE2018719), and the Advantage Discipline "Information and Communication Engineering" of Jiangsu Province, China, which are highly appreciated by the authors.

References

[1] E. Galanaki, K. Lagouvardos, V. Kotroniet, E. Flaounas, and A. Argiriou, "Thunderstorm climatology in the Mediterranean using cloud-to-ground lightning observations," *Atmospheric Research*, vol. 207, pp. 136–144, 2018.

[2] P. W. Miller and T. L. Mote, "Characterizing severe weather potential in synoptically weakly forced thunderstorm environments," *Natural Hazards and Earth System Sciences*, vol. 18, no. 4, pp. 1261–1277, 2018.

[3] U. Sonnadara, W. Jayawardena, and M. Fernando, "Climatology of lightning flash activities over Sri Lanka," *Theoretical and Applied Climatology*, vol. 137, no. 3-4, pp. 3173–3182, 2019.

[4] M. Becerra, M. Long, W. Schulz, and R. Thottappillil, "On the estimation of the lightning incidence to offshore wind farms," *Electric Power Systems Research*, vol. 157, pp. 211–226, 2018.

[5] H. Xing, X. Yangand, and J. Zhang, "Thunderstorm cloud localization algorithm and performance analysis of a three-dimensional atmospheric electric field apparatus," *Journal of Electrical Engineering and Technology*, vol. 14, no. 6, pp. 2487–2495, 2019.

[6] J. M. Wilkinson and F. J. Bornemann, "A lightning forecast for the London 2012 Olympics opening ceremony," *Weather*, vol. 69, no. 1, pp. 16–19, 2014.

[7] W. Xu, X. Feng, and H. Xing, "Modeling and analysis of adaptive temperature compensation for humidity sensors," *Electronics*, vol. 8, no. 4, p. 425, 2019.

[8] M. A. da Silva Ferro, J. Yamasaki, D. R. de Matos Pimentel, K. P. Naccarato, and M. M. F. Saba, "Lightning risk warnings based on atmospheric electric field measurements in Brazil," *Journal of Aerospace Technology and Management*, vol. 3, no. 3, pp. 301–310, 2011.

[9] A. Fort, M. Mugnaini, V. Vignoli et al., "Design, modeling, and test of a system for atmospheric electric field measurement," *IEEE Transactions on Instrumentation and Measurement*, vol. 60, no. 8, pp. 2778–2785, 2011.

[10] J. Montanya, J. Bergas, and B. Hermoso, "Electric field measurements at ground level as a basis for lightning hazard warning," *Journal of Electrostatics*, vol. 60, no. 2-4, pp. 241–246, 2004.

[11] Q. Chen, G. Weiand, and H. Wan, "Quantum inversion of thunderstorm charged model," *Chinese Journal of Geophysics*, vol. 53, no. 9, pp. 2237–2243, 2010.

[12] A. V. Frank-Kamenetsky, O. A. Troshichev, G. B. Burns, and V. O. Papitashvili, "Variations of the atmospheric electric field in the near-pole region related to the interplanetary magnetic field," *Journal of Geophysical Research Space Physics*, vol. 106, no. A1, pp. 179–190, 2001.

[13] X. Da, H. Shen, and L. Hong, "Aircraft electric field measurements: recent research status and key technologies," *Journal of the Academy of Equipment Command and Technology*, vol. 19, no. 3, pp. 80–84, 2008.

[14] M. Koto and S. Okabe, "Multipoint measurement of electric field in oil gap by using electric field measurement systems based on Kerr effect," *IEEJ Transactions on Power and Energy*, vol. 126, no. 3, pp. 321–326, 2006.

[15] H. Xing, G. He, and X. Ji, "Analysis on electric field based on three dimensional atmospheric electric field apparatus," *Journal of Electrical Engineering and Technology*, vol. 13, no. 4, pp. 1696–1703, 2018.

[16] W. Xu, C. Zhang, X. Ji, and H. Xing, "Inversion of a thunderstorm cloud charging model based on a 3d atmospheric electric field," *Applied Sciences*, vol. 8, no. 12, article 2642, 2018.

[17] J. Lopez, E. Perez, J. Herrera, D. Aranguren, and L. Porras, "Thunderstorm warning alarms methodology using electric field mills and lightning location networks in mountainous regions," in *2012 International Conference on Lightning Protection (ICLP)*, Vienna, Austria, September 2012.

[18] A. J. Illingworth and J. Latham, "Calculations of electric field growth, field structure and charge distributions in thunderstorms," *Quarterly Journal of the Royal Meteorological Society*, vol. 103, no. 436, pp. 281–295, 1977.

[19] Z. Zhao, X. Qie, T. Zhang et al., "Electric field soundings and the charge structure within an isolated thunderstorm," *Chinese Science Bulletin*, vol. 55, no. 9, pp. 872–876, 2010.

[20] H. Xing and Y. Yan, "Detection of low-flying target under the sea clutter background based on Volterra filter," *Complexity*, vol. 2018, Article ID 1513591, 12 pages, 2018.

[21] F. Leberl, "Introduction to the mathematics of inversion in remote sensing and indirect measurement," *Tectonophysics*, vol. 65, no. 3, pp. 376–378, 2013.

[22] X. Yang, H. Xing, and X. Ji, "Sound source omnidirectional positioning calibration method based on microphone observation angle," *Complexity*, vol. 2018, Article ID 2317853, 15 pages, 2018.

[23] C. C. Chen and Y. T. Cheng, "Physical analysis of a biomimetic microphone with a central-supported (c-s) circular diaphragm for sound source localization," *IEEE Sensors Journal*, vol. 12, no. 5, pp. 1504–1512, 2012.

[24] H. Xing and X. Yang, "Sound source localization fusion algorithm and performance analysis of a three-plane five-element microphone array," *Applied Sciences*, vol. 9, no. 12, article 2417, 2019.